Multi-atlas pancreas segmentation: Atlas selection based on vessel structure

Ken'ichi Karasawa[a,*], Masahiro Oda[a], Takayuki Kitasaka[b], Kazunari Misawa[c], Michitaka Fujiwara[d], Chengwen Chu[e], Guoyan Zheng[e], Daniel Rueckert[f], Kensaku Mori[g,*]

[a] *Graduate School of Information Science, Nagoya University, Furo-cho, Chikusa-ku, Nagoya, Aichi, 464-8601, Japan*
[b] *School of Information Science, Aichi Institute of Technology, Yagusa-cho, Toyota, Aichi, 470-0356, Japan*
[c] *Aichi Cancer Center, Chikusa-ku, Nagoya, Aichi, 464-8681, Japan*
[d] *Nagoya University Graduate School of Medicine, Tsurumai-cho, Showa-ku, Nagoya, Aichi, 466-8550, Japan*
[e] *Institute for Surgical Technology and Biomechanics (ISTB), University of Bern, Stauffacherstrasse 78, Bern 3014, Switzerland*
[f] *Department of Computing, Imperial College London, SW7 2AZ, UK*
[g] *Information and Communications, Nagoya University, Furo-cho, Chikusa-ku, Nagoya, Aichi, 464-8601, Japan*

Abstract

Automated organ segmentation from medical images is an indispensable component for clinical applications such as computer-aided diagnosis (CAD) and computer-assisted surgery (CAS). We utilize a multi-atlas segmentation scheme, which has recently been used in different approaches in the literature to achieve more accurate and robust segmentation of anatomical structures in computed tomography (CT) volume data. Among abdominal organs, the pancreas has large inter-patient variability in its position, size and shape. Moreover, the CT intensity of the pancreas closely resembles adjacent tissues, rendering its segmentation a challenging task. Due to this, conventional intensity-based atlas selection for pancreas segmentation often fails to select atlases that are similar in pancreas position and shape to those of the unlabeled target volume. In this paper, we propose a new atlas selection strategy based on vessel structure around the pancreatic tissue and demonstrate its application to a multi-atlas pancreas segmentation. Our method utilizes vessel structure around the pancreas to select atlases with high pancreatic resemblance to the unlabeled volume. Also, we investigate two types of applications of the vessel structure information to the atlas selection. Our segmentations were evaluated on 150 abdominal contrast-enhanced CT volumes. The experimental results showed that our approach can segment the pancreas with an average Jaccard index of 66.3% and an average Dice overlap coefficient of 78.5%.

Keywords: multi-atlas, pancreas segmentation, atlas selection, vessel structure, CT image

1. Introduction

Automated abdominal organ segmentation from three-dimensional medical images is one of the essential components for clinical applications, such as computer-aided diagnosis (CAD) (Kobatake (2007)), computer-assisted surgery (CAS) planning and navigation (Azagury et al. (2012)). Pancreatic cancer has recently been increasing globally (Ito et al. (2013)), and its mortality rate is the fourth among cancer-related deaths in Japan, 2011 (Matsuda et al. (2011)). Because pancreatic cancer is difficult to treat and has such a high mortality rate, it would be beneficial to develop systems to automatically detect the pancreatic region for radiologists (Shimizu et al. (2010)).

Among the abdominal organs, the pancreas has particularly large inter-subject variability in its position, size and shape among the population. Also, the pancreas has a thinner shape in the abdominal region compared

*Corresponding author. Tel: +81-52-789-5688
Email addresses: kkarasawa@mori.m.is.nagoya-u.ac.jp (Ken'ichi Karasawa), kensaku@is.nagoya-u.ac.jp (Kensaku Mori)
URL: http://www.mori.m.is.nagoya-u.ac.jp/wiki/ (Kensaku Mori)

with other abdominal organs. The CT intensity of the pancreatic region is very similar to its neighboring structures, i.e. the stomach wall, duodenum and small/large intestines. These properties render the segmentation of the pancreas relatively challenging.

1.1. Related works

In recent years, many organ segmentation methods have been proposed (Summers (2016)). Among them, multi-atlas segmentation schemes have been widely utilized for abdominal organ segmentation (Iglesias and Sabuncu (2015)). Early explorations of multi-atlas segmentation are reported for brain tissues from magnetic resonance (MR) images (Rohlfing et al. (2004); Heckemann et al. (2006); Lötjönen et al. (2010)). Common to all these methods is that they all adopt certain type of global registration, e.g. affine registration, to obtain atlases to a target image space. Aljabar et al. (2009) demonstrated that atlas selection was effective in improvement of segmentation accuracy for brain MR images. Wolz et al. (2013) applied the locally weighted atlas selection scheme to multiple abdominal organ segmentation from contrast-enhanced CT images. This approach presents a free-form deformation (FFD) (Rueckert et al. (1999)) based hierarchical multi-atlas registration and segmentation framework. Chu et al. (2013) performs Markov random field (MRF)-based registration (Glocker et al. (2008)) and globally spatially divided hierarchical construction of probabilistic atlas for abdominal multi-organ segmentation.

These multi-atlas approaches for abdominal organ segmentation have achieved good segmentation performances on relatively large organs, e.g. the liver. However, as for the segmentation accuracy of the pancreas, it is still significantly lower than other abdominal organs. One of the main reasons is that the selection of atlases with high similarity in the pancreatic region tends to fail due to the fact that the tissues surrounding the pancreas region have similar CT intensity. Also, the pancreatic shape and position have large inter-subject variability. These pancreatic properties cause the atlas-to-target registration to be trapped in local minima. Wang et al. (2014) uses patch-based segmentation with a label fusion scheme using intensity and spatial context. Tong et al. (2015) also uses voxel-wise local atlas selection to train a patch dictionary. However, these types of patch selections also consider only intensity similarity between image patches, and therefore have a high risk of mis-selection of similar patches as shown in Bai et al. (2015).

1.2. Contribution of this paper

In this paper, we propose a new atlas selection strategy based on vessel structure to overcome the aforementioned atlas selection failure and demonstrate its application to multi-atlas pancreas segmentation. The main motivation of utilizing vessel structure for the atlas selection is that each abdominal organ is generally close to certain vessels, e.g. the pancreatic body is running along the splenic vein and the head is along the superior mesenteric vein. A schematic illustration of anatomical structure surrounding the pancreas is shown in Fig. 1. Different from vessels inside the brain region, these vessels have larger diameters and can be utilized for organ position information. For example, Farag et al. (2014a) considers detecting three abdominal structures (splenic vein, superior mesenteric vein, and their confluence point) as landmarks for pancreas localization. Other SSM-based approaches with anatomical landmark detection of organs and vessels (Shimizu et al. (2010); Hammon et al. (2013); Okada et al. (2015)) demonstrate the combination of SSM, and these anatomical landmarks could be more effective for the target segmentation.

The main contribution of this paper is summarized as follows: We propose a method that uses vasculature around the pancreas in the atlas selection. This procedure is intended to reduce the mis-selection of similar atlas caused by CT intensity. To perform this, we introduce two types of applications of vessel structure. Atlases are selected based on vessel structure image. One application utilizes vessel structure binarized image and the other utilizes vessel structure enhanced image. In the light of the criterion in atlas selection, there are many ways for atlas selection. For example, Aljabar selected atlases based on age (Aljabar et al. (2009)). Cordier selected atlases using intensity distribution (Cordier et al. (2015)). The paper by Iglesias and Sabuncu (Iglesias and Sabuncu (2015)) surveys atlas selection criteria. In terms of atlas selection criteria, the proposed method can be classified as the method utilizing anatomical structure information (including the splenic vein) in atlas selection.

In Section 2, we explain our multi-atlas segmentation pipeline in detail. In Section 3, CT images used in the experiments and segmentation results are described. We discuss advantages and disadvantages of our method in

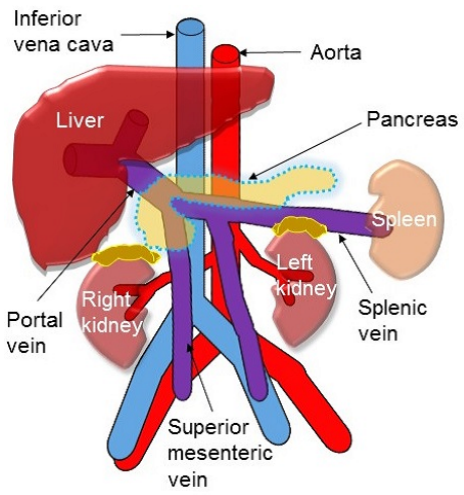

Figure 1: Schematic illustration of anatomical structure surrounding the pancreas.

Section 4 as well as comparison with other state-of-the-art approaches. This paper is concluded in Section 5.

2. Method

2.1. Overview

We briefly explain our pancreas segmentation method step-by-step (Fig. 2). First, spatial standardization of the abdominal region and extraction of the pancreatic region are performed for all available atlas data. Each atlas data includes CT volume and its manually labeled abdominal organs (liver, spleen, pancreas, and both kidneys). Then, the vessel structure around the pancreas region is automatically detected and vessel structure images are generated. After that, atlas-to-target registration is carried out between cropped pancreatic regions. The vessel structure images of each atlas data and its associated CT volume are warped with the resulting deformation fields. Here, we have two types of vessel structure images. One is a binarized image whose voxels have 1 in the vessel region and others 0. The other is an enhanced image whose voxels have a positive enhancement value in the vessel region and others 0. Then, we select atlas data based on similarity between the deformed vessel images. Using the selected atlases, a probability map of each target of the unlabeled CT volume is generated. A graph cut optimization is performed to combine probability and intensity prior of each organ. The input to our pipeline is an unlabeled CT volume and the output is the labeled image of that CT volume.

2.2. Atlas data preparation

2.2.1. Spatial standardization of abdominal region

First, spatial standardization of all atlas data is executed as preprocessing. The spatial standardization is useful to reduce the inter-subject variability of positions and sizes of abdominal organs. This process consists of simple image processing such as translation and scaling of the abdomen. The detailed process is shown in Chu et al. (2013) and a short summary is presented in Appendix A. This process produces normalized atlas data whose image size and resolution are the same in all the atlas data.

2.2.2. Pancreas VOI computation

We compute the volume of interest that contains the whole pancreas region in each atlas data. We call this volume of interest the PVOI (pancreas volume of interest). PVOI is defined as a cuboid region whose edge sizes are all the same. PVOI size is defined as a maximum size that covers all the pancreas regions stored in all atlas data. The center of a PVOI is computed from the positional information of the liver. First, we compute

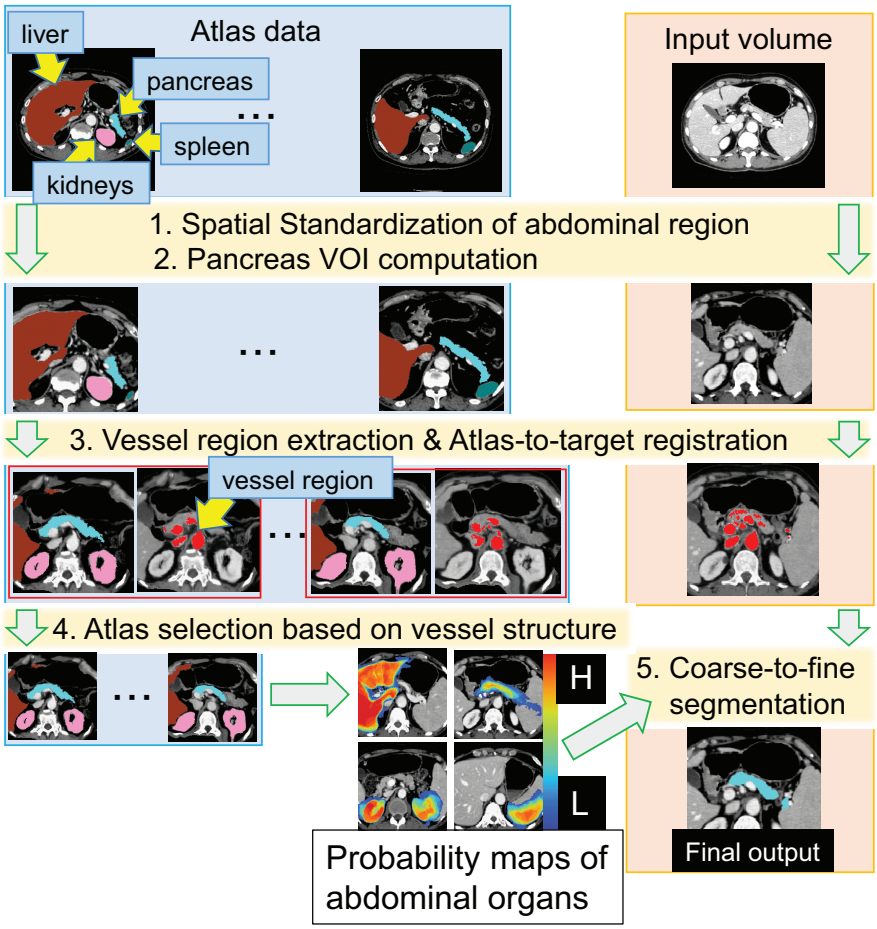

Figure 2: Proposed pipeline of multi-atlas pancreas segmentation. Left and right side indicate the process of atlas data set and unlabeled input CT volume, respectively.

the liver and the pancreas centers for each atlas from the liver and the pancreas regions stored in the atlas dataset. These centers can be computed as the geometrical average of voxel positions of each region. Then, we compute the average vector from the liver center to the pancreas center as

$$\overline{\Delta} = \frac{1}{N}\sum_{n=1}^{N}\{\mathbf{O}_P^{(n)} - \mathbf{O}_L^{(n)}\}, \tag{1}$$

where N is the number of atlas images stored in the dataset, and $\mathbf{O}_P^{(n)}$ and $\mathbf{O}_L^{(n)}$ are the positions of the pancreas and the liver. The PVOI center $\mathbf{O}_P^{(n)}$ is estimated by the following equation:

$$\tilde{\mathbf{O}}_P^{(n)} \equiv \mathbf{O}_L^{(n)} + \overline{\Delta} \approx \mathbf{O}_P^{(n)}. \tag{2}$$

The PVOI radius r is determined so that PVOIs with a size of $2r$ cover all the pancreas regions for all the atlas data. The PVOI can be expressed as

$$\begin{aligned}\mathcal{R} = \{\mathbf{x} \mid \quad & |x - \tilde{O}_{P_x}| \le r, \\ & |y - \tilde{O}_{P_y}| \le r, \\ & |z - \tilde{O}_{P_z}| \le r \quad \}.\end{aligned} \tag{3}$$

As stated above, a PVOI can be obtained from the liver center information. Liver regions can be stably obtained

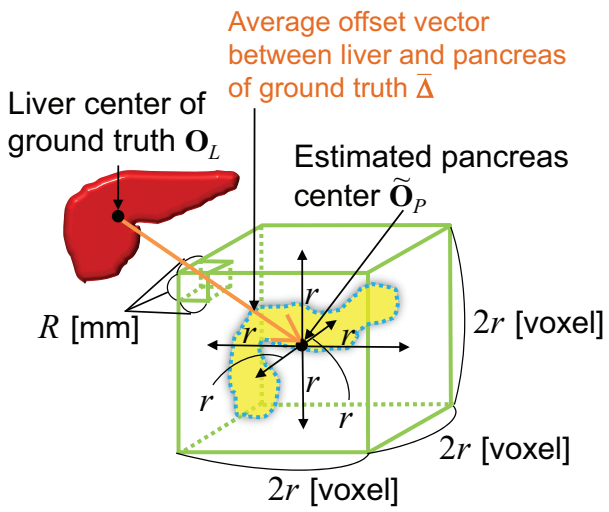

Figure 3: Illustration of pancreas VOI computation. Using liver center of ground truth O_L and average offset vector $\bar{\Delta}$, the pancreas center is estimated as $\tilde{\mathrm{O}}_P$. Then pancreas VOI centered at $\tilde{\mathrm{O}}_P$ is extracted as above.

manually from a contrasted CT volume and are located next to the pancreas. Since the PVOI must also be obtained for an input CT data, this approach can easily identify a PVOI of an input data from the liver information stably obtained from an input data. Figure 3 represents a graphical illustration of the PVOI computation.

2.3. Vessel region extraction

This step computes vessel regions within each extracted PVOI. The vessel structure images are generated for all CT images including the atlas and input images. The target vessel regions include the splenic vein (SV), superior mesenteric vein (SMV), aorta (AO), inferior vena cava (IVC), portal vein (PV). Below, we propose two types of vessel images for atlas selection.

2.3.1. Vessel structure binarized image (VBI)

A vessel structure binarized image (VBI) is computed within a PVOI. In this image, voxels of the vessel region are expressed as 1 and others are 0. Therefore, the vessel structure binarized image is given by

$$V_B(\mathbf{x}) = \begin{cases} 1, & \text{if } \mathbf{x} \text{ is a vessel voxel,} \\ 0, & \text{otherwise.} \end{cases} \tag{4}$$

Figure 4 (a) shows an example of the automatically extracted vessel structure binarized image in a transverse slice. Our procedure to generate the vessel structure binarized image is decomposed into the following two steps: AO detection and SV detection.

A set of AO seed points is explored in a transverse slice first. This is simply found by applying a morphological operator, thresholding, and region labeling. A labeled region with maximum area and roundness is selected as AO seed points. Region growing is performed from the seed points with a spherical component to detect AO voxels.

Next, SV detection begins with searching for the hilum point of the spleen using the ground truth of the spleen. We generate the ground truth of the spleen of each CT image by manual tracing. This point plays a role in the connection between the spleen and the SV. To detect the hilum point, we utilize a multi-scale line enhancement filter with Hessian analysis detailed in Sato et al. (1998). A set of detected voxels with high enhancement values inside the spleen are selected as seed points of region growing. Again, region growing is performed with a similar setting to earlier to detect SV voxels from the hilum via SV to the end of SMV.

Finally, we integrate the outputs of the AO detection and the SV detection to generate a vessel structure

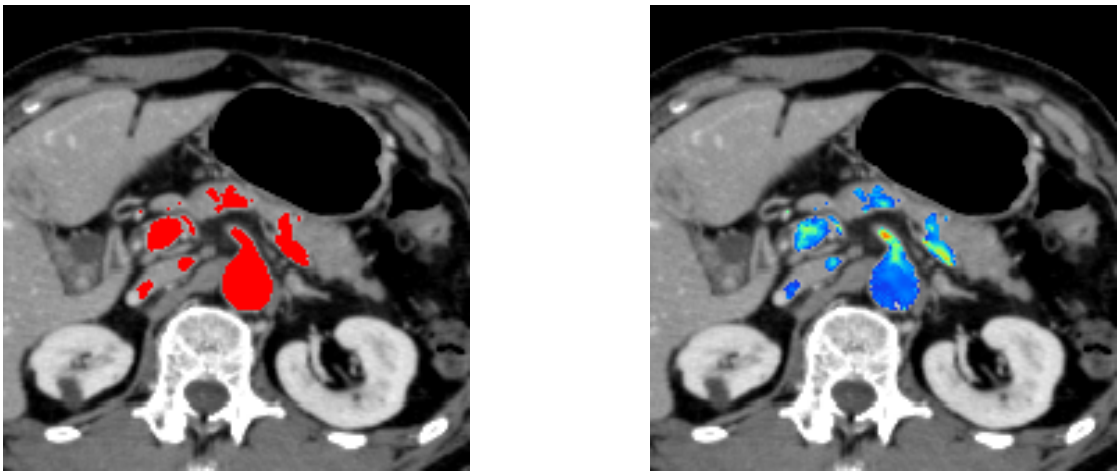

(a) (b)

Figure 4: (a) Automatically extracted vessel structure binarized image overlapped with its CT slice. The vessel region is colored red. (b) Vessel structure enhanced image. Color code indicates a low enhancement with blue and high enhancement with red.

binarized image $V_B(\mathbf{x})$.

2.3.2. Vessel structure enhanced image (VEI)

A vessel structure enhanced image represents vessel voxels within a PVOI as a positive enhancement value, and the others as 0. To generate the vessel structure enhanced image, we employ a multi-scale line enhancement filter (Sato et al. (1998)). We utilize the vessel structure binarized image $V_B(\mathbf{x})$ as a masking region to enhance the vessel-like structures within it. The vessel structure enhanced image is given by

$$V_E(\mathbf{x}) = \begin{cases} w \cdot \max\limits_{1 \le i \le m} \{\sigma_i^2 \cdot \lambda_{123}(\mathbf{x}; \sigma_i)\}, & \text{if } \mathbf{e}_1^{\mathrm{T}} \mathbf{u}_z \le \tau, \\ \max\limits_{1 \le i \le m} \{\sigma_i^2 \cdot \lambda_{123}(\mathbf{x}; \sigma_i)\}, & \text{otherwise.} \end{cases} \quad (5)$$

Here $\sigma_i \equiv i \cdot \sigma_1$ and $\sigma_1, \lambda_{123}(\cdot), m$ represent a standard deviation of Gaussian function, output value of multi-scale line enhancement filter, and step size of the enhancement filter, respectively. These notations are employed in the conventional multi-scale line enhancement filter (Sato et al. (1998)). The $\lambda_{123}(\cdot)$ is give as

$$\lambda_{123}(\mathbf{x}; \sigma_i) = \begin{cases} |\lambda_2| + \lambda_1, & \text{if } \lambda_3 < \lambda_2 < \lambda_1 \le 0, \\ |\lambda_2| - \lambda_1, & \text{if } \lambda_3 < \lambda_2 < 0 \\ & \quad < \lambda_1 < |\lambda_2|, \\ 0, & \text{otherwise.} \end{cases} \quad (6)$$

λ_1, λ_2, and λ_3 represent the first, second, and third eigenvalue of the Hessian matrix at $\mathbf{x}$ with a σ_i, respectively.

We introduce the following four new mathematical symbols into the conventional multi-scale line enhancement filter: $w, \mathbf{e}_1, \mathbf{u}_z, \tau$ in Eq. (5) are a weight coefficient, unit vector of the first eigenvector of the Hessian matrix centered at $\mathbf{x}$ with scale of σ_i, unit vector of the head-to-foot direction, and threshold value, respectively. This paper utilizes the anatomical knowledge that the SV running along the pancreatic region is basically orthogonal to the head-to-foot axis, where the formed angle $\ge \theta_{\mathrm{const}}$. The weight w controls the strength to emphasize the SV. Figure 4 (b) shows an example of the vessel structure enhanced image obtained by applying Eq. (5). Figure 5 shows 3D visualizations of the vessel structure enhanced images.

2.4. Atlas-to-target registration

Each atlas PVOI is aligned to the unlabeled PVOI with the nonrigid registration technique based on Markov random field (MRF) optimisation (Glocker et al. (2008)). After the MRF optimization, each atlas PVOI including the vessel images $V_B(\mathbf{x}), V_E(\mathbf{x})$ is warped using the deformation field. The atlas-to-target registration is performed within the whole PVOI.

Figure 5: 3D visualizations of vessel structure enhanced images by the volume rendering technique. Regions having high vessel enhanced values are displayed as opaque region.

2.5. Atlas selection based on vessel structure image

A similarity between the vessel images of each atlas and unlabeled CT is measured, and atlases with the N_h highest similarities are selected. Each selected atlas is weighted with that similarity and averaged to generate a probability map of each organ $M_l(\mathbf{x})$, where $l \in \{\text{liver}, \text{spleen}, \text{pancreas}, \text{both kidneys}, \text{background}\}$.

We propose two types of atlas selection schemes based on different image similarity measurements of the vessel structure. One utilizes the Jaccard index (Jaccard (1901)), which assesses an overlap between vessel regions of an input PVOI and an atlas PVOI.

Another utilizes normalized cross correlation (NCC) (Bracewell (1965)). NCC also measures a similarity between vessel regions of an input PVOI and an atlas PVOI. NCC places much importance on the vessel-like structures with the line enhancement value.

2.6. Pancreas region segmentation

Coarse-to-fine pancreas segmentation using the probability maps $M_l(\mathbf{x})$ is performed. This process combines maximum a posterior (MAP) estimation (Levitan and Herman (1987)) and refinement with multi-class graph cut optimization (Boykov et al. (2001); Boykov and Kolmogorov (2004)).

We use an expectation maximization (EM) algorithm (Dempster et al. (1977)) to estimate a probability density function $P(I(\mathbf{x})|\theta_l)$ of CT intensity of each organ l for voxel $\mathbf{x}$ within the non-zero region of $M_l(\mathbf{x})$, except for a background. Here, θ_l indicates a set of parameters that the EM algorithm infers for organ l. Each organ region is modeled as a mixture of three Gaussian distributions. Each distribution represents a low-intensity, high-intensity, and organ region, respectively. A low-intensity region mainly includes the air and fat tissues while the high-intensity region includes vessel and bone regions. This is helpful in order to exclude the non-organ regions included in the probability map and makes each estimation more accurate. The MAP estimation is computed by the following formula of

$$l^*(I(\mathbf{x})) \approx \arg\max_l P(I(\mathbf{x})|\theta_l) M_l(\mathbf{x}), \tag{7}$$

where $l^*(I(\mathbf{x}))$ represents an estimated optimal organ label of voxel $\mathbf{x}$ with intensity value of $I(\mathbf{x})$.

The estimation is done by multi-class graph cut optimization in the same manner as Wolz et al. (2013) (Appendix B).

3. Data and Results

3.1. Material

150 abdominal CT scans acquired from 36 female and 114 male subjects were used for the experiments. All scans were acquired between 2004 and 2009 at Nagoya University hospital by a TOSHIBA Aquilion 64 scanner and obtained under typical clinical protocols for the purpose of laparoscopic resection of the stomach and gallbladder glands or colon. 141 subjects had early or ad-

Table 1: CT specification.

Slice size [pixels]	512 × 512
Slice number [slices]	263 ∼ 1061
Pixel spacing [mm]	0.546 ∼ 0.820
Slice thickness [mm]	0.400 ∼ 0.800

Table 2: Acquisition parameters.

X-ray tube voltage [kV]	120
X-ray tube current [mAs]	350 ∼ 400
Starting point (patient age < 60)	25s delayed after injection
Starting point (patient age ≥ 60)	7s after intensity of aorta is over 80 H.U.

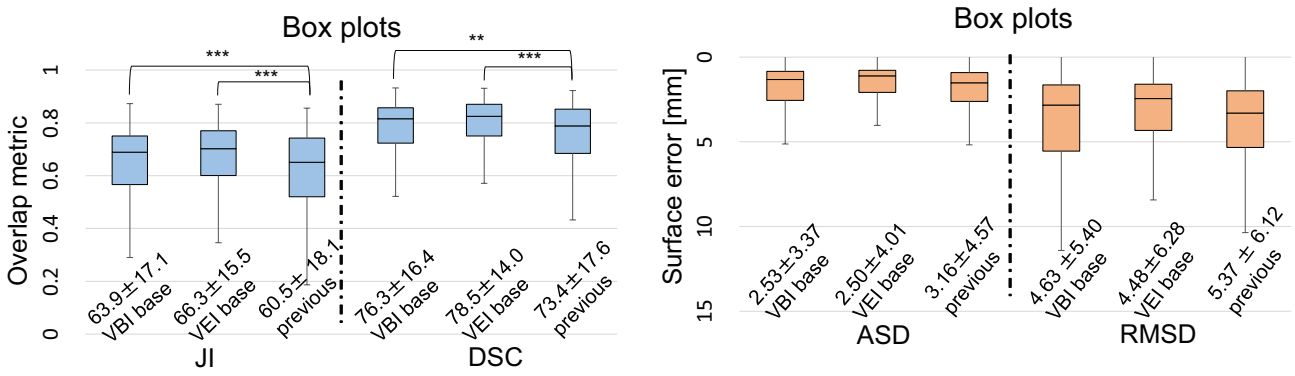

Figure 6: Box plots of four evaluation metrics of the proposed segmentation and previous one (Karasawa et al. (2015)). From left to right, proposed segmentation based on VBI, VEI, and previous one in each column. A black horizontal line of each box plot indicates a median value. ** and *** represent that there exists a significant difference ($p < 0.01$) and stronger significant difference ($p < 0.001$) between two methods, respectively. Bottom value of each box plot represents average ± standard deviation. (a) Box plots of Jaccard index and Dice coefficient. (b) Box plots of average surface distance and root-mean square distance.

vanced gastric cancer, one subject had cholecystitis cancer and eight subjects had colorectal cancer. All subjects were aged between 26 and 84 years with a mean age of 62.8 ± 12.0. CT specification and acquisition parameters are summarized as Tables 1 and 2.

Manual rating was performed for the ground truth data of the liver, spleen, pancreas and the kidneys. All 150 subjects were segmented by one out of three trained raters. Segmentation of the ground truth images is based on interactive region growing, where a spherical element is utilized to prevent excess segmentation of a target region, or graph-cut segmentation, where a set of foreground and background voxels is manually set as seed points. After the semi-automated segmentation, manual correction of all the segmentations was performed on all the slices of right-to-left, ventral-to-back, and head-to-foot directions.

In the experiments shown in this paper, we utilized liver regions manually traced. This trace can be replaced with automated method such as the one developed by Wolz et al. (2013). The center is computed from the liver region.

Four types of measurements are used for segmentation evaluation: Jaccard index (JI) (Jaccard (1901)), DSC similarity coefficient (DSC) (Dice (1945)), average symmetric surface distance (ASD), and root-mean average symmetric surface distance (RMSD) (Heimann et al. (2009)). JI and DSC measurements evaluate the overlap between the ground truth and the segmentation result of the pancreas. The others evaluate a surface distance error between them.

We fixed the parameters as $r = 84, w = 2.0, \tau = 0.25, \sigma_1 = 1.0, m = 10$. These values were experimentally determined. We performed the segmentation ex-

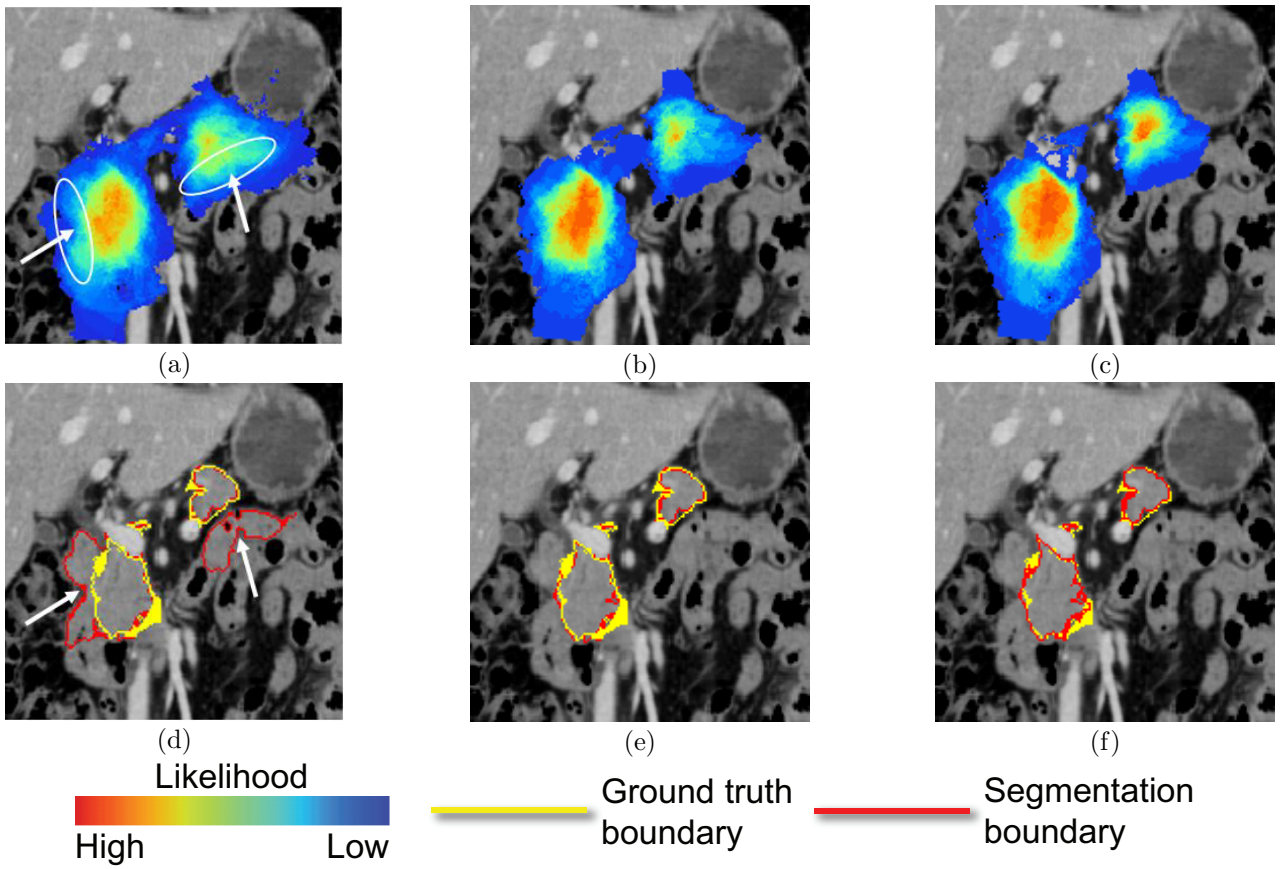

Figure 7: Example where the segmentation accuracy is improved by proposed method compared to the previous one. Each image represents a coronal slice in the same position. From left to right, a probability map and the corresponding segmentation contour overlapped with the ground truth contour of the conventional, VBI-based, and VEI-based methods, respectively. (a) - (c) indicate the probability maps. Color code represents low probability with blue and high probability with red. (d) - (f) indicate the corresponding segmentation contours and ground truth contours. Ground truth boundary is traced in yellow and segmentation boundary in red. Segmentation performance is 34.2%, 76.9%, and 80.2% with respect to JI, respectively.

periments using the atlas selection with $N_h = 20$. This number is selected based on previous experiences.

3.2. Experimental results

Leave-one-out cross validation was utilized for the performance evaluation. All experiments were executed on servers equipped with an Intel Xeon Dual or Quad Core 1.86 $\sim$ 3.07 GHz CPU. The overall runtime per CT volume takes between two $\sim$ four hours.

Two types of the atlas selections described in Section 2.5 are performed separately and evaluated. For simplicity, we refer to vessel structure binarized image as VBI and vessel structure enhanced image as VEI.

Figure 6 (a) and (b) show box plots of the evaluation metrics of the proposed segmentation and the conventional one (Karasawa et al. (2015)), respectively. In Fig. 6, both VBI- and VEI-based segmentation much outperform the conventional one in terms of JI and DSC measurements. We performed a statistical pair-wise two-tailed t-test in terms of JI, DSC, ASD, and RMSD. In the t-test in terms of JI and DSC between the VBI-based method and the conventional method, the VBI-based segmentations were significant with $p = 2.26 \times 10^{-4} < 0.001$, $1.25 \times 10^{-3} < 0.01$, respectively. In the t-test in terms of JI and DSC between the VEI-based method and the conventional method, the VEI-based segmentations

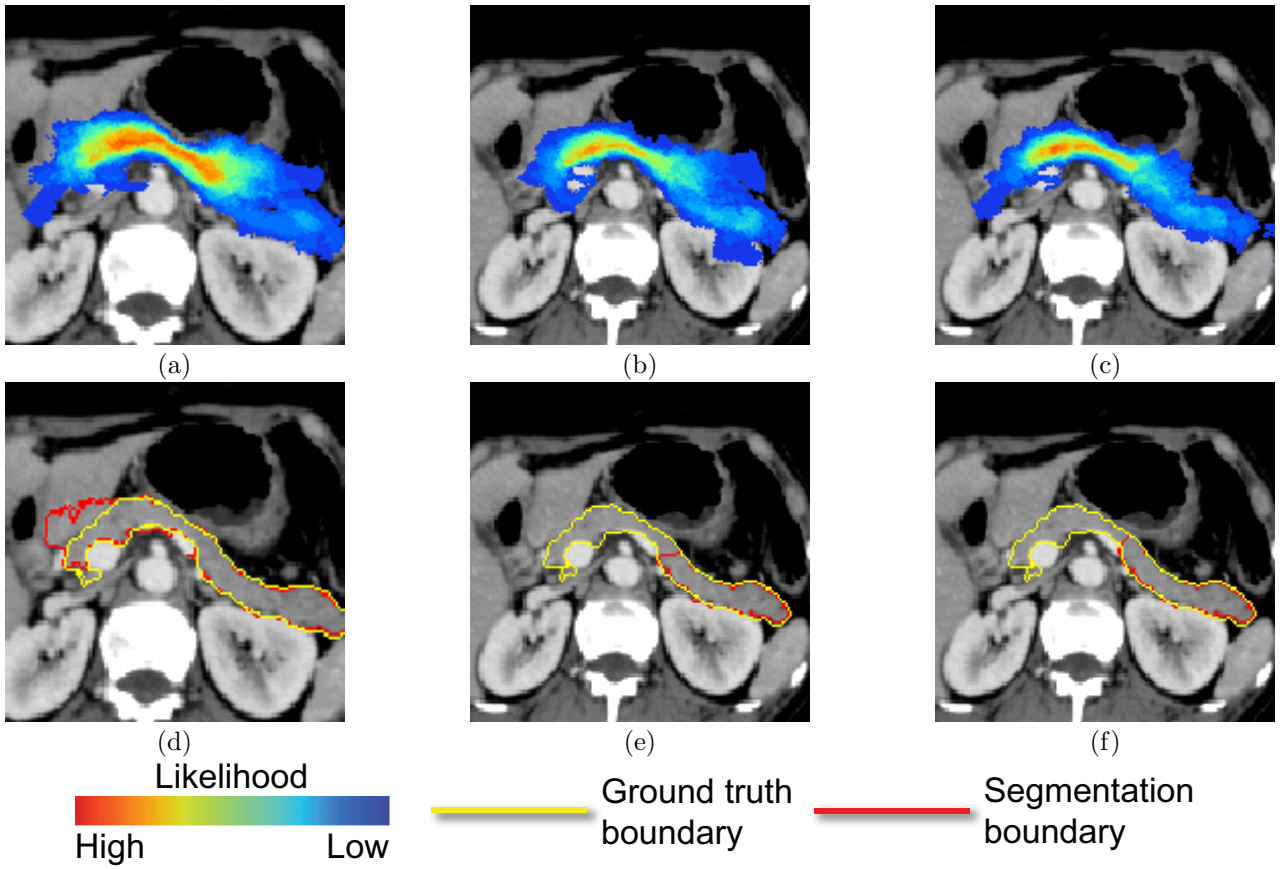

Figure 8: Example where the segmentation accuracy is reduced by the proposed method compared to the previous one. Each image represents a transverse slice in the same position. From left to right, a probability map and the corresponding segmentation contour overlapped with the ground truth contour of the conventional, VBI-based, and VEI-based methods, respectively. (a) - (c) indicate the probability maps. Color code represents low probability with blue and high probability with red. (d) - (f) indicate the corresponding segmentation contours and ground truth contours. Ground truth boundary is traced in yellow and segmentation boundary in red. Segmentation performance is 64.0%, 29.3%, and 31.1% with respect to JI, respectively.

were significant with $p = 5.74 \times 10^{-9}$, $2.96 \times 10^{-7} < 0.001$, respectively. As shown in Fig. 6 (b), there is no statistical significance between the proposed and the previous methods on the surface error measurements. The reason for this will be discussed in Section 4.

Figure 7 shows an improved case with the probabilistic map and the corresponding segmentation contour together with the ground truth contour. Figure 7 (a) - (c) show the probabilistic map generated by the conventional, VBI-based, and VEI-based methods, respectively. Figure 7 (d) - (f) show the contours of the ground truth and the segmentation result of the conventional, VBI-based, and VEI-based methods, respectively. From left to right, segmentation performance is 34.2%, 76.9%, and 80.2% with respect to JI, respectively. The white arrows in (a) point to areas where the probability is relatively higher in the duodenum and small intestine regions with similar intensity to the pancreas. False positives to these regions have occurred in (d). However, we can see in (b) and (c) that the probability of these regions is lowered by the proposed VBI- and VEI-based segmentation. This resulted in the elimination of the false positives.

Figure 8 shows a worse case with the probabilistic map and the corresponding segmentation contour together with the ground truth contour. Figure 8 (a) - (c) indicate the probabilistic map generated by the con-

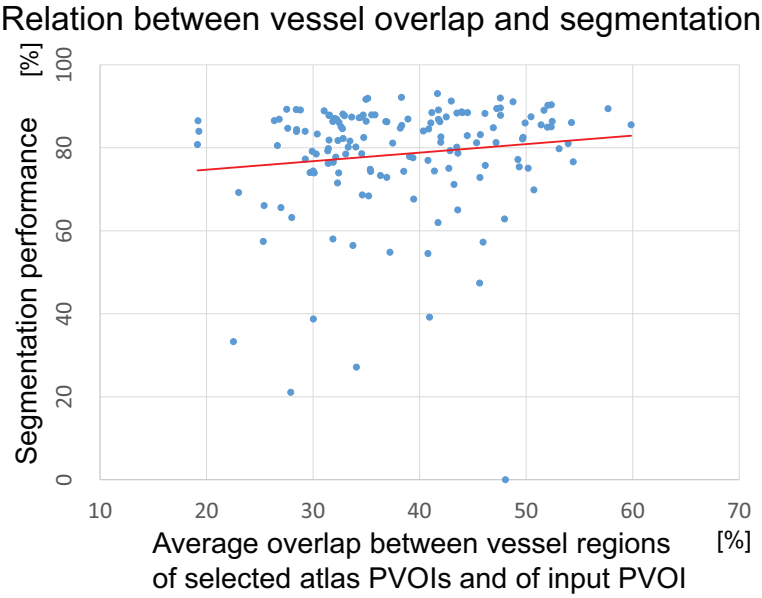

Figure 9: Scatter plot that describes relation between vessel region overlap within a PVOI and pancreas segmentation accuracy. The overlap is measured with DSC. Horizontal axis represents average overlap between vessel regions of selected atlas PVOIs and of input PVOI. Vertical axis represents average overlap between pancreas regions of selected atlas PVOIs and of input PVOI. Green arrows show that the higher the average overlap between vessel regions of selected atlas PVOIs and of input PVOI becomes, the smaller the dispersion of segmentation performance.

ventional, VBI-based, and VEI-based methods, respectively. Figure 8 (d) - (f) indicate the contours of the ground truth and the segmentation result of the conventional, VBI-based, and VEI-based methods, respectively. From left to right, the segmentation performance is 64.0%, 29.3%, and 31.1% with respect to JI, respectively. For this case, we can see that the probability map has a better shape than the previous (a); however, the segmentation results of the proposed methods have false negatives in the pancreatic head region. This implies that the regularization term in the coarse-to-fine segmentation is important and should be automatically adjusted for every CT volume.

A scatter plot that describes a relation between vessel region overlap within PVOI and pancreas segmentation accuracy is shown in Fig. 9. Standard deviations of pancreas centroid along x-, y-, and z-axes are shown in Fig. 10. Examples of cases who have relatively large surface distance error ($>$ 10 mm with ASD) are shown in Fig. 11.

4. Discussion

Through our experiments using vessel structure-based atlas selection, we were able to obtain better performances on the pancreas segmentation. In particular, we obtained better segmentation performance using vessel structure enhancement, which places more emphasis on the splenic vein region. From this reason, we can conclude that the atlas selection based on vessel structure is much more effective in selecting atlases with similar pancreatic shape and position to that of an input CT volume.

Figure 9 indicates a scatter plot that describes a relation between vessel region overlap and segmentation performance. The vessel region overlap in the horizontal axis represents an average overlap between vessel regions of selected N atlas PVOIs and of input PVOI. The vertical axis represents the segmentation accuracy assessed with DSC. From the plot, we can observe the following: one is that the vessel structure-based atlas selection for multi-atlas pancreas segmentation has a positive ef-

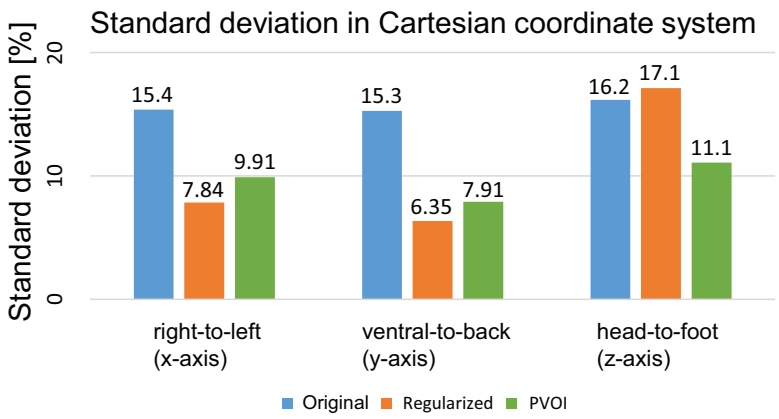

Figure 10: Standard deviations of pancreas centroid along x-, y-, and z-axes in original (blue), standardized (orange), and cropped PVOI space (green). Lower standard deviations are obtained in the x- and y-axes by the abdominal spatial regularization. The next PVOI extraction reduces much standard deviation in the z-axis.

fect on selecting atlases with similar pancreas shape and position. The other is that this atlas selection scheme is effective in elimination of the dispersion of the segmentation performance. As shown by the red regression line in this figure, there exists a weak positive correlation (=0.126) between the average vessel overlap and the pancreas segmentation performance. However, we can also observe that the variability of segmentation accuracy is amplified in the low vessel overlap region while it gets smaller in the high vessel overlap region.

We performed the spatial standardization of the abdominal region to relieve the inter-subject variability of the body trunk size and position, followed by the PVOI extraction to localize the pancreatic region more precisely. Figure 10 demonstrates that we were successful in eliminating standard deviations in the x-, y-, and z-directions by the abdominal spatial regularization and PVOI extraction. Less variability of the pancreas position and shape in the PVOI contributes to reducing the local minima of the atlas-to-target image registration to the pancreas region of an input CT volume. Therefore, this lower variability of the standard deviations in the three directions makes the registration to the pancreas more precise.

Table 3 shows a comparison with existing state-of-the-art works on pancreas segmentation performance. The first row shows the segmentation performance using the VBI-based or VEI-based atlas selection. The second row shows the performance evaluated on the same data set used in our experiments. The third row shows the performance evaluated on a different data set from ours. This table shows the pancreas segmentation accuracies. From this table, we can see that the proposed VBI- and VEI-based atlas selection approaches outperform any other state-of-the-art work with respect to JI and DSC overlap. The experimental result of Jiang et al. (2013) outperforms ours; however, their method was only evaluated on 10 cases and requires manual input of seed points. In contrast, our segmentation pipeline is fully automated and requires no manual delineation.

This paper is focused on pancreas region segmentation utilizing pancreas-specific atlas selection. Atlas selection was performed by considering splenetic arteries. Although the proposed method is tuned for pancreas segmentation, the similar idea can be utilized for segmentation of the kidney, which is characterized by renal arteries.

Future works mainly include the following six points. While we obtained better segmentation performance in terms of JI and DSC than most of the state-of-the-art methods shown in Table 3, our segmentation pipeline still has much higher computational burden compared with other approaches based on machine learning. This point is a main disadvantage of our method to be im-

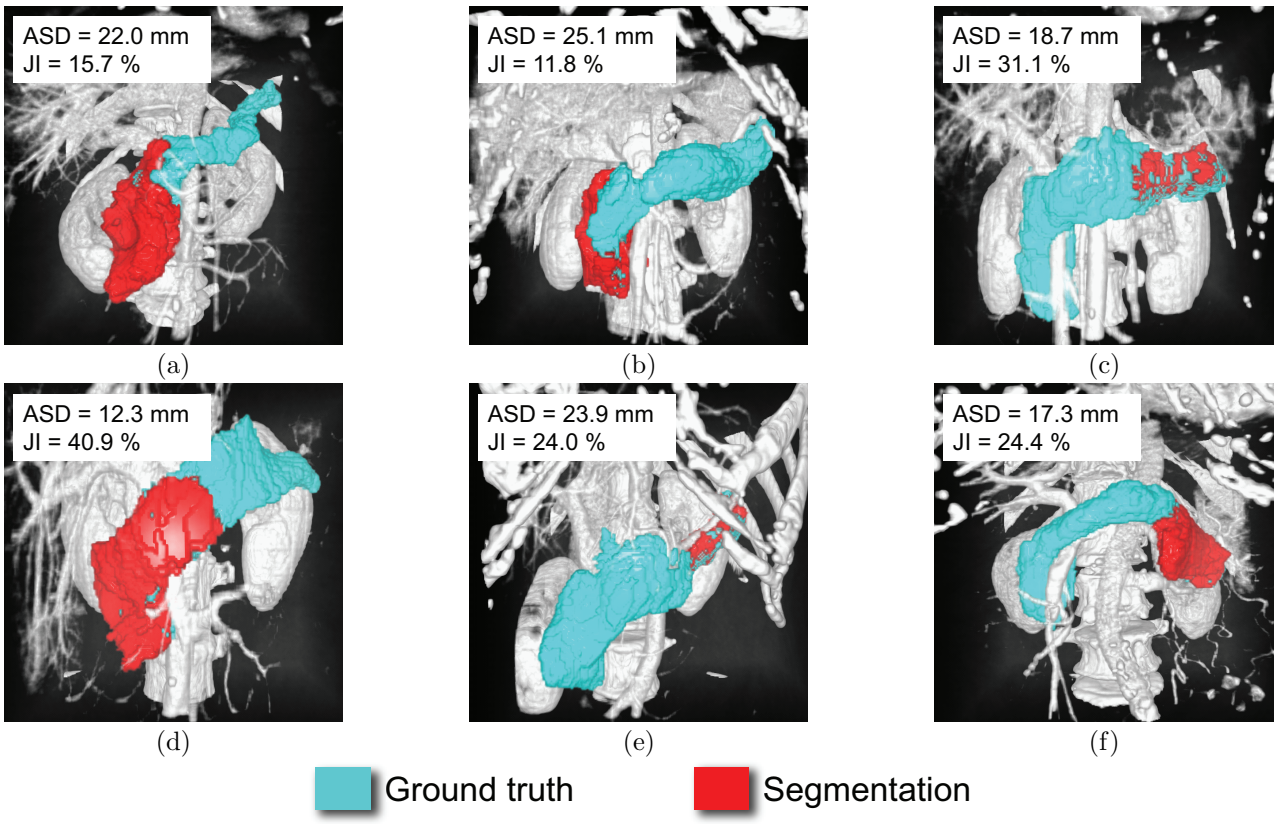

Figure 11: This figure shows six cases who have relatively large surface distance error ($>$ 10 mm with ASD) compared with region overlap metric. Each figure indicates a ground truth (blue) and its segmentation result (red) whose segmented region only has a part of the pancreas. These segmentation results become a main cause of the deterioration of the surface distance error metric like ASD and RMSD.

proved in the future. This is mainly caused by the atlas-to-target nonrigid registration. The computational complexity can be an issue in the application to the CAD system of pancreatic cancer, considering surgeons may wish to diagnose the cancer on the spot.

We used an in-house dataset of CT volumes in our evaluation. To compare the segmentation accuracy with the previous methods, use of the same dataset is important. We plan to evaluate our method on available open datasets on which previous methods have been evaluated.

Figure 11 shows examples which have relatively large surface distance error ($>$ 10 mm with ASD). As shown here, with our method there were cases whose surface distance errors were more deteriorated than the overlap measurements. This indicates that atlases selected by the proposed method failed to represent the pancreas shape in some cases. Shape robustness of atlas need to be improved. Incorporating a shape prior or shape condition using an organ statistical shape model into the smoothness term of the graph cut of the proposed method will allow us to consider the correspondence between two pancreas parts, e.g. the pancreas tails, of the pancreas statistical shape model and of the pancreas region of an input CT volume. Also, the performance measures such as JI, DSC, ASD, RMSD, or others are needed to be selected by clinical application demands. The proposed method may have satisfying performance for some applications.

Throughout the experiments, the atlas selection number $N_h = 20$ is fixed. Other atlas selection numbers, e.g. 30, should be tested to explore the impact on the segmentation performance. Also, we need to automatically determine an optimal number for every input CT volume.

Table 3: Comparison table of pancreas segmentation from CT scan. First row shows proposed methods, second row shows segmentation performance of other groups using the same dataset as ours, and third row shows the segmentation performance of other groups using a different dataset from ours. The table only shows the segmentation performance (JI, DSC, ASD) on the pancreas. We use the following brief symbols for each organ: heart (H), stomach (ST), esophagus (E), liver (L), spleen (S), pancreas (P), kidneys (RK, LK), gallbladder (G), portal vein (PV), aorta (AO), inferior vena cava (IVC). Also, we use the following brief symbols for each CT phase: multiple phase (M), portal venous phase (P), arbitrary phase (A), non-contrast enhanced phase (N).

Method	# of data	CT phase	Segmentation target	Runtime [h/case]	Performance on pancreas segmentation		
					JI [%]	DSC [%]	ASD [mm]
VBI base	150	P	P	$2 \sim 4$	63.9 ± 17.1	76.3 ± 16.4	2.53 ± 3.37
VEI base	150	P	P	$2 \sim 4$	66.3 ± 15.5	78.5 ± 14.0	2.50 ± 4.01
Wolz et al. (2013)	150	P	L,S,P,RK,LK	3	55.5 ± 17.1	69.6 ± 16.7	3.72 ± 4.36
Chu et al. (2013)	100	P	L,S,P,RK,LK	-	54.6 ± 15.9	69.1 ± 15.3	1.88 ± 0.64
Wang et al. (2014)	100	P	L,S,P,RK,LK	14	-	65.5 ± 18.6	-
Karasawa et al. (2015)	150	P	P	-	60.5 ± 18.1	73.4 ± 17.6	3.16 ± 4.57
Tong et al. (2015)	150	P	L,S,P,RK,LK	$0.5 \sim 2$	56.9 ± 15.2	71.1 ± 14.7	-
Kitasaka et al. (2008)	22	M	P	-	visual assessment: good 12, normal 6, bad 4		
Shimizu et al. (2007)	10	N	H,ST,E L,S,P,RK,LK G,PV,AO,ICV	-	32.5	-	-
Shimizu et al. (2010)	98	M	P	45 [min]	57.9	-	-
Hammon et al. (2013)	40	P	P	20.4 [min]	61.2 ± 9.08	-	1.70 ± 0.71
Jiang et al. (2013)	10	P	P	$0.195 \sim 0.199$ [s/slice]	-	88.4	-
Farag et al. (2014b)	80	P	P	2 ± 3 [min]	57.2 ± 25.4	68.8 ± 25.6	-
Roth et al. (2015)	82	P	P	55 (training) $1 \sim 3$ [min] (testing)	-	68 ± 10	-
Roth et al. (2016)	82	P	P	$2 \sim 3$ [min]	-	78.0 ± 8.2	0.60 ± 0.55
Okada et al. (2013)	87	A	L,S,P,RK,LK G,AO,IVC	-	52.8	-	-
Okada et al. (2015)	134	A	L,S,P,RK,LK G,AO,IVC	-	60.4 ± 16.7	73.4 ± 15.1	2.77 ± 2.40
Saito et al. (2016)	140	M	P,S	213 [s]	62.3 ± 19.5	74.4 ± 20.2	-

The VBI- and VEI-based atlas selection methods use the Jaccard index (JI) and normalized cross correlation (NCC) as image similarity to select similar atlases from the data set. It is worth to explore other image similarity metrics like normalized mutual information (NMI) and average surface distance (ASD).

We utilized the vessel structure information in the PVOI in the research and obtained the best segmentation performance using the atlas selection based on it. However, we only focused on the vasculature around the pancreatic region. On this point, we should investigate the effectiveness of the whole abdominal vessel structure with a large field-of-view for similar atlas selection of other abdominal organs, e.g. the liver. It's also promising to use abdominal anatomical landmarks for similar atlas selection because they also have the anatomical information that gives a prior of organ position.

Some processes in the proposed method utilize manually segmented regions of organs including liver and spleen. Also, the spatial standardization of abdominal region process Chu et al. (2013) includes organ segmentation process. These segmentation results affect pancreas segmentation accuracy of the proposed method. The relation between them need to be clarified. Full automation of these organ segmentation processes will be necessary.

5. Conclusion

We proposed a multi-atlas pancreas segmentation method based on vessel structure around the pancreas. We also utilized the spatial standardization of the abdominal region and extraction of the pancreatic region (PVOI) to make the variability of the pancreas centroid smaller, which contributes to the lower local minima of the image registration. From the experimental results, we achieved 66.3% average JI and 78.5% average DSC overlap using the multi-atlas segmentation pipeline using vessel structure enhanced image (VEI)-based atlas selection. This VEI emphasizes more on the splenic vein region, which runs along the pancreatic region. We can conclude that the vessel structure-based atlas selection is effective in selecting atlases with similar pancreas shape and position to that of an input CT volume.

Acknowledgment

The authors would like to express gratitude to our supervisors and colleagues for constructive suggestions and advice. Parts of this research were supported by the MEXT, the JSPS KAKENHI Grant Numbers 25242047, 26108006, 26560255, JSPS Joint Research Projects "Turning medical image collection into anatomical knowledge wisdom based on image recognition and understanding and its application to computer-assisted diagnosis and surgery", and the Kayamori Foundation of Informational Science Advancement.

Appendix A

Spatial standardization of the abdominal region is simply performed by image scaling and translation using

$$\mathbf{x}' = \mathbf{x}\mathbf{T_1}\mathbf{S}\mathbf{T_2}, \tag{8}$$

where $\mathbf{T_1}$ and $\mathbf{T_2}$ represent two translation matrices and $\mathbf{S}$ represents a scaling matrix. A voxel $\mathbf{x}$ in the original space is projected into a new position $\mathbf{x}'$ in the standardized space.

For the purpose of finding the matrices, we utilize a body trunk region (which includes abdominal cavity, anatomical tissues inside the body, and body surface), lung regions, and kidney regions. These regions are extracted with the combination of some image processing techniques such as region growing and 26-neighbor labeling. The kidney and the lung regions are roughly segmented by thresholding and connected component processes. Since we utilized the contrasted CT images in the experiment, the kidney can be extracted by simple thresholding process. The lung regions also can be extracted by thresholding and connected component. We define the matrices as

$$\mathbf{T_1} = \begin{bmatrix} 1 & 0 & 0 & 0 \\ 0 & 1 & 0 & 0 \\ 0 & 0 & 1 & 0 \\ -C_x & -C_y & -B_z & 1 \end{bmatrix}, \tag{9}$$

$$\mathbf{S} = \begin{bmatrix} \frac{\overline{w}}{w} & 0 & 0 & 0 \\ 0 & \frac{\overline{h}}{h} & 0 & 0 \\ 0 & 0 & \frac{\overline{d}}{d} & 0 \\ 0 & 0 & 0 & 1 \end{bmatrix}, \tag{10}$$

$$\mathbf{T_2} = \begin{bmatrix} 1 & 0 & 0 & 0 \\ 0 & 1 & 0 & 0 \\ 0 & 0 & 1 & 0 \\ \overline{C}_x & \overline{C}_y & \overline{B}_z & 1 \end{bmatrix}, \tag{11}$$

where $\overline{w}, \overline{h}$ indicates an average width and height of the bounding box of the body trunk, respectively. $\overline{C}_x, \overline{C}_y$ indicates an average center position in the transverse plane. $\overline{d}$ is an average distance between the bottoms of the lungs and the kidneys. $\overline{B}_z$ is an average bottom position of the lungs. These six values are computed ahead of the experiments. The unit of the values is millimeters. For an unlabeled CT volume, the same six values of w, h, C_x, C_y, d, B_z are calculated in the same manner.

Appendix B

In the multi-class graph cut, we define an energy function as

$$E(\mathbf{L}) = \sum_{\mathbf{x}\in\mathcal{R}} R(\mathbf{x}) + \lambda \sum_{(\mathbf{x},\mathbf{x}')\in\mathcal{E}} B(\mathbf{x},\mathbf{x}'), \tag{12}$$

where $\mathbf{L}$ shows an array of the label disposition estimated by Eq. (7). λ is a regularized coefficient. $R(\cdot)$ and $B(\cdot,\cdot)$ are a data term and smoothness term, respectively. The data term $R(\cdot)$ represents a binary disagreement between the estimated labels $l^*_{\mathbf{x}}$ and each organ label l and is defined as

$$R(\mathbf{x}) = \begin{cases} 0, & \text{if } l = l^*_{\mathbf{x}}, \\ 1, & \text{otherwise.} \end{cases} \tag{13}$$

The smoothness term $B(\cdot,\cdot)$ measures a penalty of discontinuity between voxels and is given as

$$B(\mathbf{x},\mathbf{x}') = \begin{cases} 0, & \text{if } l_{\mathbf{x}} = l_{\mathbf{x}'}, \\ \frac{1}{(1+|I(\mathbf{x})-I(\mathbf{x}')|)\cdot \mathrm{d}(\mathbf{x},\mathbf{x}')}, & \text{otherwise}, \end{cases} \quad (14)$$

where $\mathcal{E}$ represents a set of neighboring voxels defined as $\mathcal{E} = \{(\mathbf{x},\mathbf{x}')|\mathbf{x} \in \mathcal{R}, \mathbf{x}' \in \mathcal{N}^{\mathbf{x}}\}$. $\mathcal{N}^{\mathbf{x}}$ is a set of voxels connecting to $\mathbf{x}$ with 26-neighbor. The function $\mathrm{d}(\cdot,\cdot)$ measures Euclidean distance between two voxels.

References

Aljabar, P., Heckemann, R.A., Hammers, A., Hajnal, J.V., Rueckert, D., 2009. Multi-atlas based segmentation of brain images: Atlas selection and its effect on accuracy. NeuroImage 46(3), 726–738.

Azagury, D.E., Ryou, M., Shaikh, S.N., San José Estépar, R., Lengyel, B.I., Jagadeesan, J., Vosburgh, K.G., Thompson, C.C., 2012. Real-time computed tomography-based augmented reality for natural orifice transluminal endoscopic surgery navigation. British Journal of Surgery 99(9), 1246–1253.

Bai, W., Shi, W., Ledig, C., Rueckert, D., 2015. Multi-atlas segmentation with augmented features for cardiac MR images. Medical Image Analysis 19(1), 98–109.

Boykov, Y., Kolmogorov, V., 2004. An experimental comparison of min-cut/max-flow algorithms for energy minimization in vision. IEEE Transactions on Pattern Analysis and Machine Intelligence 26(9), 1124–1137.

Boykov, Y., Veksler, O., Zabih, R., 2001. Fast approximate energy minimization via graph cuts. IEEE Transactions on Pattern Analysis and Machine Intelligence 23(11), 1222–1239.

Bracewell, R., 1965. Pentagram notation for cross correlation. The Fourier Transform and Its Applications. New York: McGraw-Hill 46, 243.

Chu, C., Oda, M., Kitasaka, T., Misawa, K., Fujiwara, M., Hayashi, Y., Nimura, Y., Rueckert, D., Mori, K., 2013. Multi-organ segmentation based on spatially-divided probabilistic atlas from 3D abdominal CT images. Medical Image Computing and Computer-Assisted Intervention, Lecture Notes in Computer Science 8150, 165–172.

Cordier, N., Delingette, H., Ayache, N., 2015. A patch-based approach for the segmentation of pathologies: Application to glioma labelling. IEEE Transactions on Medical Imaging 35, 1066–1076.

Dempster, A.P., Laird, N.M., Rubin, D.B., 1977. Maximum likelihood from incomplete data via the EM algorithm. Journal of the Royal Statistical Society 39(1), 1–38.

Dice, L.R., 1945. Measures of the amount of ecologic association between species. Ecology 26(3), 297–302.

Farag, A., Liu, J., Summers, R.M., 2014a. Automatic segmentation of abdominal vessels for improved pancreas localization. Proc. SPIE Medical Imaging 9037.

Farag, A., Lu, L., Turkbey, E., Liu, J., Summers, R.M., 2014b. A bottom-up approach for automatic pancreas segmentation in abdominal CT scans. Medical Image Computing and Computer-Assisted Intervention, Lecture Notes in Computer Science 8676, 103–113.

Glocker, B., Komodakis, N., Tziritas, G., Navab, N., Paragios, N., 2008. Dense image registration through MRFs and efficient linear programming. Medical Image Analysis 12(6), 731–741.

Hammon, M., Cavallaro, A., Erdt, M., Dankerl, P., Kirschner, M., Drechsler, K., Wesarg, S., Uder, M., Janka, R., 2013. Model-based pancreas segmentation in portal venous phase contrast-enhanced CT images. Journal of Digital Imaging 26(6), 1082–90.

Heckemann, R.A., Hajnal, J.V., Aljabar, P., Rueckert, D., Hammers, A., 2006. Automatic anatomical brain MRI segmentation combining label propagation and decision fusion. NeuroImage 33(1), 115–126.

Heimann, T., Ginneken, B.V., Styner, M.A., Arzhaeva, Y., Aurich, V., Bauer, C., Beck, A., Becker, C., Beichel, R., Bekes, G., Bello, O., Binnig, G., Bischof, H., Bornik, E., Cashman, P.M.M., Chi, Y., Cordova, A., Dawant, B.M., Fidrich, M., Furst, J.D., Furukawa, D., Grenacher, L., Hornegger, J., Kainmuller, D., Kitney, R.I., Kobatake, H., Lamecker, H., Lange, T., Lee, J., Lennon, B., Li, R., Li, S., Meinzer, H.P., Nemeth, G., Raicu, D.S., Rau, A.M., Rikxoort, E.M.V., Rousson, M., Rusko, L., Saddi, K.A., Schmidt, G., Seghers, D., Shimizu, A., Slagmolen, P., Sorantin, E., Soza, G.,

Susomboon, R., Waite, J.M., Wimmer, A., Wolf, I., 2009. Comparison and evaluation of methods for liver segmentation from CT datasets. IEEE Transactions on Medical Imaging 28(8), 1251–1265.

Iglesias, J.E., Sabuncu, M.R., 2015. Multi-atlas segmentation of biomedical images: A survey. Medical Image Analysis 24, 205–219.

Ito, M., Makino, N., Ueno, Y., 2013. Glucose intolerance and the risk of pancreatic cancer. Translational Gastrointestinal Cancer 2(4), 223–229.

Jaccard, P., 1901. Étude comparative de la distribution florale dans une portion des alpes et des jura (in French). Bulletin de la Societe Vaudoise des Sciences Naturelles 37(142), 547–579.

Jiang, H., Hanqing, T., Fujita, H., 2013. A hybrid method for pancreas extraction from CT image based on level set methods. Computational and Mathematical Methods in Medicine doi:http://dx.doi.org/10.1155/2013/479516.

Karasawa, K., Oda, M., Hayashi, Y., Nimura, Y., Kitasaka, T., Misawa, K., Fujiwara, M., Rueckert, D., Mori, K., 2015. Pancreas segmentation from 3D abdominal CT images using patient-specific weighted-subspatial probabilistic atlases. Proc. SPIE Medical Imaging 9413.

Kitasaka, T., Sakashita, M., Mori, K., Suenaga, Y., Nawano, S., 2008. A method for extracting pancreas regions from four-phase contrasted 3D abdominal CT images. International Journal for Computer-Assisted Radiology and Surgery (IJCARS) 3, Suppl. 1, S40–42.

Kobatake, H., 2007. Future CAD in multi-dimensional medical images: - project on multi-organ, multi-disease CAD system -. Computerized Medical Imaging and Graphics 31(4–5), 258–266.

Levitan, E., Herman, G.T., 1987. A maximum a posteriori probability expectation maximization algorithm for image reconstruction in emission tomography. IEEE Transactions on Medical Imaging 6(3), 185–192.

Lötjönen, J.M.P., Wolz, R., Koikkalainen, J.R., Thurfjell, L., Waldemar, G., Soininen, H., Rueckert, D., 2010. Fast and robust multi-atlas segmentation of brain magnetic resonance images. NeuroImage 49(3), 2352–2365.

Matsuda, T., Ajiki, W., Marugame, T., Ioka, A., Tsukuma, H., Sobue, T., 2011. Population-based survival of cancer patients diagnosed between 1993 and 1999 in Japan: a chronological and international comparative study. Japanese Journal of Clinical Oncology 41, 40–51.

Okada, T., Linguraru, M.G., Hori, M., Summers, R.M., Tomiyama, N., Sato, Y., 2013. Abdominal multi-organ CT segmentation using organ correlation graph and prediction-based shape and location priors. Medical Image Computing and Computer-Assisted Intervention, Lecture Notes in Computer Science 8151, 275–282.

Okada, T., Linguraru, M.G., Hori, M., Summers, R.M., Tomiyama, N., Sato, Y., 2015. Abdominal multi-organ segmentation from CT images using conditional shape-location and unsupervised intensity priors. Medical Image Analysis doi:http://dx.doi.org/10.1016/j.media.2015.06.009.

Rohlfing, T., Russakoff, D.B., Maurer, C.R., 2004. Performance-based classifier combination in atlas-based image segmentation using expectation-maximization parameter estimation. IEEE Transactions on Medical Imaging 23(8), 983–994.

Roth, H.R., Farag, A., Lu, L., Turkbey, E.B., Summers, R.M., 2015. Deep convolutional networks for pancreas segmentation in CT imaging. Proc. SPIE Medical Imaging 9413.

Roth, H.R., Lu, L., Farag, A., Sohn, A., Summers, R.M., 2016. Spatial aggregation of holistically-nested networks for automated pancreas segmentation. Medical Image Computing and Computer-Assisted Intervention, Lecture Notes in Computer Science 9901, 451–459.

Rueckert, D., Sonoda, L.I., Hayes, C., Hill, D.L., Leach, M.O., Hawkes, D.J., 1999. Nonrigid registration using free-form deformations: application to breast MR images. IEEE Transactions on Medical Imaging 18(8), 712–721.

Saito, A., Nawano, S., Shimizu, A., 2016. Joint optimization of segmentation and shape prior from level-set-based statistical shape model, and its application to the automated segmentation of abdominal organs. Medical Image Analysis 28, 46–65.

Sato, Y., Nakajima, S., Shiraga, N., Atsumi, H., Yoshida, S., Koller, T., Gerig, G., Kikinis, R., 1998. Three-dimensional multi-scale line filter for segmentation and visualization of curvilinear structures in medical images. Medical Imaging Analysis 2(2), 143–168.

Shimizu, A., Kimoto, T., Kobatake, H., Nawano, S., Shinozaki, K., 2010. Automated pancreas segmentation from three-dimensional contrast-enhanced computed tomography. International Journal of Computer Assisted Radiology and Surgery 5, 85–98.

Shimizu, A., Ohno, R., Ikegami, T., Kobatake, H., Nawano, S., Smutek, D., 2007. Segmentation of multiple organs in non-contrast 3D abdominal CT images. International Journal of Computer Assisted Radiology and Surgery 2(3–4), 135–142.

Summers, R.M., 2016. Progress in fully automated abdominal CT interpretation. American Journal of Roentgenology 207, 67–79.

Tong, T., Wolz, R., Wang, Z., Gao, Q., Misawa, K., Fujiwara, M., Mori, K., Hajnal, J.V., Rueckert, D., 2015. Discriminative dictionary learning for abdominal multi-organ segmentation. Medical Image Analysis 23(1), 92–104.

Wang, Z., Bhatia, K.K., Glocker, B., Marvao, A., Dawes, T., Misawa, K., Mori, K., Rueckert, D., 2014. Geodesic patch-based segmentation. Medical Image Computing and Computer-Assisted Intervention, Lecture Notes in Computer Science 8673, 666–673.

Wolz, R., Chu, C., Misawa, K., Fujiwara, M., Mori, K., Rueckert, D., 2013. Automated abdominal multi-organ segmentation with subject-specific atlas generation. IEEE Transactions on Medical Imaging 32(9), 1723–1730.